

Fast and Memory-Efficient Voronoi Diagram Construction on Triangle Meshes

Yipeng Qin Hongchuan Yu Jianjun Zhang

National Centre for Computer Animation, Bournemouth University, UK

Abstract

Geodesic based Voronoi diagrams play an important role in many applications of computer graphics. Constructing such Voronoi diagrams usually resorts to exact geodesics. However, exact geodesic computation always consumes lots of time and memory, which has become the bottleneck of constructing geodesic based Voronoi diagrams. In this paper, we propose the window-VTP algorithm, which can effectively reduce redundant computation and save memory. As a result, constructing Voronoi diagrams using the proposed window-VTP algorithm runs 3-8 times faster than Liu et al.'s method [LCT11], 1.2 times faster than its FWP-MMP variant and more importantly uses 10-70 times less memory than both of them.

Categories and Subject Descriptors (according to ACM CCS): I.3.5 [Computer Graphics]: Computational Geometry and Object Modeling—Curve, surface, solid, and object representations

1. Introduction

Computing geodesic-metric-based Voronoi diagrams on triangle meshes works as a foundation for various applications in computer graphics, including remeshing [PC06, LCT11], surface reconstruction [PM15] and point pattern analysis [LCT11], etc. In these applications, geodesics are used as the distance metric because they reflect the intrinsic properties of surfaces and are invariant to isometric deformations. To construct accurate Voronoi diagrams, Liu et al. [LCT11] employed the MMP algorithm [SSK*05] to it. Compared to other exact geodesic algorithms (e.g. ICH [XW09], VTP [QHY*16]), the MMP algorithm has a unique feature: all the propagated windows are stored and trimmed on edges. The distinct advantage is to bring necessary geodesic information to edges for Voronoi diagram construction. However, as the MMP algorithm always consumes lots of time and memory, it has become the bottleneck of constructing geodesic based Voronoi diagrams. Recently, Xu et al. [XWL*15] proposed the FWP-MMP algorithm as an accelerated version of the MMP algorithm. But it still occupies too much memory to be applied to large scale models.

The main deficiency of the MMP algorithm is to propagate all windows to edges, which results in lots of computation on redundant windows, and even invalid ones. To speed up geodesic computation and save memory, we propose to use the Vertex-sorted Triangle Propagation (VTP) exact geodesic algorithm [QHY*16], which can identify and remove the maximum invalid windows. Moreover for the Voronoi diagram over a mesh, the boundaries of Voronoi cells only occupy a small number of triangles on it (Fig. 1). Thus,

most of the windows are redundant in constructing Voronoi diagrams.

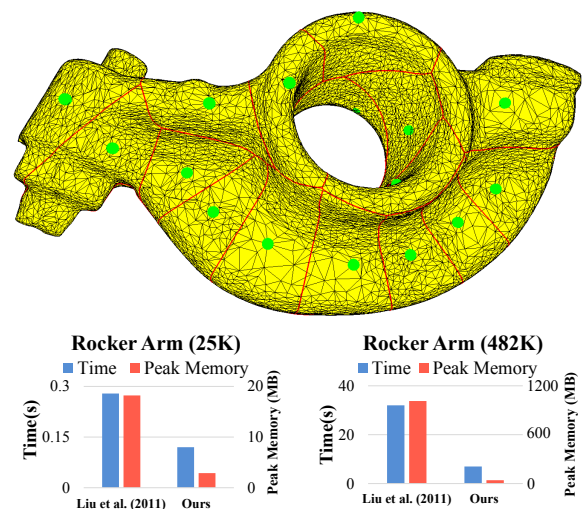


Figure 1: Our algorithm outperforms Liu et al.'s method [LCT11] in both running time and peak memory. The upper figure shows the Voronoi diagram on the Rocker Arm model (25K faces). The lower charts compare the performance of Liu et al.'s method and ours on two Rocker Arm models (25K and 482K faces).

This paper aims to reduce redundant computation so as to save time and memory as shown in Fig. 1. To this end, the Redundant Window Removal (RWR) process is proposed to remove redundant windows during the construction of a Voronoi diagram, and is involved in our *window*-VTP algorithm by selectively retaining windows on edges. The key point is to detect and remove redundant windows simultaneously with the geodesic wavefront propagation.

In summary, the contributions of this paper are:

- A novel Redundant Window Removal (RWR) method to remove redundant windows during the Voronoi diagram construction.
- The high efficiency of Voronoi diagram construction. Our method runs 3-8 times faster than Liu et al.'s method [LCT11], 1.2 times faster than its FWP-MMP variant and more importantly uses 10-70 times less memory than both of them, which is ideal for large scale models.

2. Related Work

Discrete Geodesic Computation. Mitchell et al. first formulated the computation of geodesic distances on triangle meshes as the *Discrete Geodesic Problem* (DGP) [MMP87]. To solve DGP quickly, PDE-based approximation algorithms have been proposed [KS98, CWW13]. However, these algorithms are sensitive to mesh quality and may produce potentially large errors [LCT11]. Thus, we prefer the exact geodesic algorithms as used in this paper.

The *window propagation framework* is employed by all the state-of-the-art exact geodesic algorithms [SSK*05, XW09, XWL*15, QHY*16]. In this framework, geodesics are encoded in a geometric data structure called *window* and propagated from the source over the mesh surface. To improve its performance, windows are sorted by a priority queue and propagated according to their distances in a continuous-Dijkstra style. During propagation, effective rules are applied to remove the redundant windows that cannot define geodesics, e.g. the window pruning rule [QHY*16]. Among these algorithms, the ICH algorithm [XW09], the FWP-CH algorithm [XWL*15] and the VTP algorithm [QHY*16] aim to compute geodesic distances of vertices. Thus, propagated windows are not stored on edges in these algorithms. On the other hand, the MMP algorithm [SSK*05] and the FWP-MMP algorithm [XWL*15] retain all propagated windows on edges and trim them into non-overlapping ones. Hence, the geodesic distance of a point within one triangle can be computed.

Voronoi Diagram Construction. The construction of Voronoi diagrams is studied in various metric spaces like Euclidean space [CM07, HR08] and Non-Euclidean spaces, e.g. spheres [NLC02], hyperbolic spaces [OT95], and Riemannian manifolds [OI03]. Refer to [Aur91] for a detailed survey.

In computer graphics, geodesic-metric-based Voronoi diagrams usually lie on top of triangular meshes. Kimmel and Sethian proposed the fast marching method [KS98] to compute such Voronoi diagrams [KS99]. However, since it is based on PDE, potentially large errors may occur on bad triangulated meshes. To compute Voronoi diagrams accurately, Liu et al. [LCT11] used the MMP algorithm for exact geodesic distance computation. Their method is extended by [XLS*14] to compute polyline-sourced Voronoi diagrams.

3. Redundant Window Removal (RWR)

Since the boundaries of Voronoi cells only cross a minority of the meshes' triangles, most of the windows stored on edges are redundant. Thus, this section aims to remove such windows which occupy a large amount of memory during the Voronoi diagram construction.

3.1. Preliminaries

For a triangular mesh M , its Voronoi diagram is a set of Voronoi cells partitioning M . As Fig. 2 shows, the boundaries separating Voronoi cells are closed curves spread over a small number of triangles. The definitions of Voronoi cells and their boundaries are presented as follows:

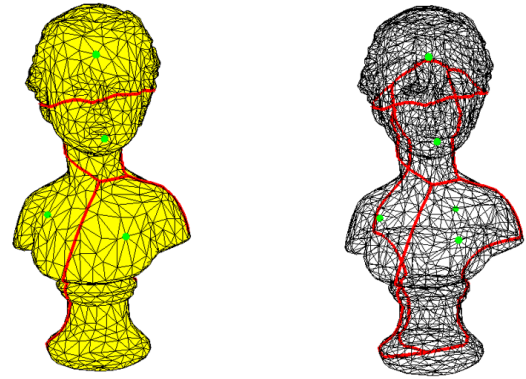


Figure 2: Voronoi diagram on the Buste model (3K faces). Left: Voronoi diagram on the rendered model. Right: Voronoi diagram on the wireframe model. The green points are sources. The red curves are the boundaries of Voronoi cells.

Voronoi Cell Definition [LCT11]. For a given set of source points s_0, s_1, \dots, s_n on mesh M , let $D_{s_i}(p)$ be the geodesic distance from source s_i to point p on M . Consequently, the Voronoi cell (VC) of each source point is defined as:

$$VC(s_i) = \{p | D_{s_i}(p) \leq D_{s_j}(p), i \neq j, p \in M\}$$

Voronoi Boundary Definition. With the Voronoi cell definition above, the boundaries of Voronoi cells are formed by the collection of points q satisfying:

$$\exists i, j \text{ and } \forall k \text{ such that } D_{s_i}(q) = D_{s_j}(q) \leq D_{s_k}(q), i \neq j \neq k \quad (3.1)$$

In this paper, geodesics on edges are encoded in “windows”, which are used as the primitives for wavefront propagation in the state-of-the-art exact geodesic algorithms [SSK*05, XW09, XWL*15, QHY*16]. The definition of a window is presented as follows:

Window Definition. As Fig. 3 shows, a window w is located on edge AB , all the geodesic paths in w are from the same source s_i or

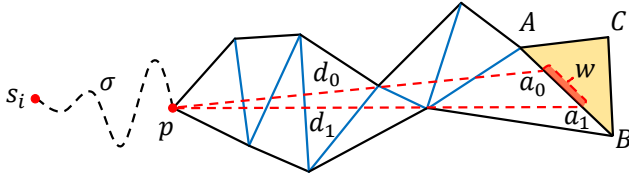


Figure 3: Illustration of the window structure.

pseudo-source p and share the same triangle strip. Therefore, w is defined as $w = (\Delta ABC, a_0, a_1, p, d_0, d_1, \sigma, s_i)$, where ΔABC stands for the triangle it enters and AB is the edge where w resides. Two scalar parameters, a_0 and a_1 , mark the two endpoints of w , which lies on the edge AB . Every window w is created by the source vertex s_i or a pseudo source, which must be a saddle vertex. Here, p represents the projection of the pseudo source on the plane determined by ΔABC , and d_0, d_1 are the distances from a_0, a_1 to p respectively. σ denotes the geodesic distance from the pseudo source to the source vertex s_i .

Redundant Window Definition. As Fig. 4 shows, suppose q is the intersection point of an edge and a Voronoi boundary. Then, q must satisfy the condition Eq.3.1 and is shared by two adjacent windows originating from two different sources respectively. The triangles occupied by the Voronoi boundaries always contain such intersection points. That is, a *valid* triangle contains windows propagated from *different* sources. Otherwise, this triangle is *invalid*. In terms of windows, the redundant primitives on a mesh are defined as below.

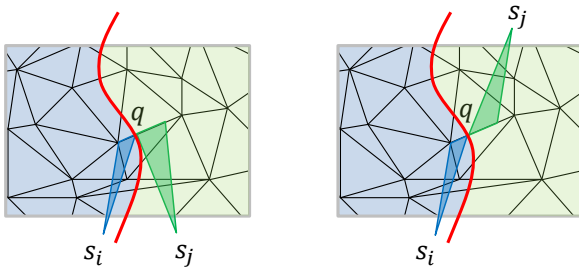


Figure 4: Illustration of intersections between mesh edges and Voronoi cell boundaries. The left Voronoi cell (in blue) is from source s_i and the right one (in green) is from source s_j . The red curve denotes the boundary between them. Point q is the intersection shared by two windows from s_i and s_j respectively that $D_{s_i}(q) = D_{s_j}(q)$. The two figures show two configurations of the source positions.

Definition 3.1 Given a mesh M with computed geodesics, the redundant primitives on M are (Fig. 5):

- **Redundant triangle.** A triangle is redundant if all the windows on its three edges are from the same source.
- **Redundant edge.** An edge is redundant if both adjacent triangles are redundant triangles.

- **Redundant window.** A window is redundant if it resides on a redundant edge.

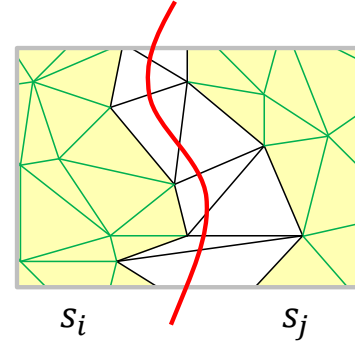


Figure 5: Illustration of redundant primitives, including redundant triangles (yellow) and redundant edges (green).

3.2. Redundant Windows Removal (RWR)

Definition 3.1 can be directly used to identify redundant windows after the termination of geodesic computation on a mesh. However, too much memory have been consumed. To avoid it, the redundant windows must be identified and removed as early as possible *during* the geodesic computation. To this end, we define the **inactive region** as follows:

Definition 3.2 An **inactive region** is a region behind the geodesic wavefront, in which all the windows will be no longer updated.

In other words, the geodesic distances of points in some inactive region have already determined. To depict the inactive region, it is necessary to first briefly address the monotonicity of window propagations.

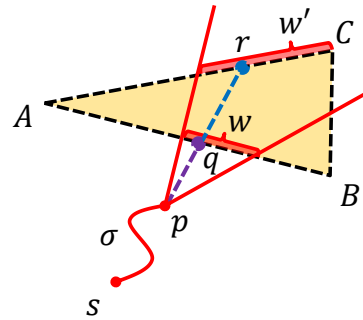


Figure 6: Illustration of the monotonicity for window propagations. Point r (blue) resides in the window w' propagated from w , segment \overline{pr} intersects edge AB at point q (purple).

Monotonicity. Mitchell et al. [MMP87] proposed the “continuous Dijkstra” technique to organize geodesic wavefront propagation from near to far *monotonically*. Herein, the wavefront consists of all the windows to be propagated and these windows are managed by a priority queue. In the priority queue, the priority of a window

w is defined as $-d_{\min}(w)$, i.e. the negative minimum distance of a window. As Fig. 6 shows, if w' is a child window propagated from w , we have:

$$d_{\min}(w') = \min(\sigma + \|\overline{p\bar{r}}\|) \geq \min(\sigma + \|\overline{p\bar{q}}\|) \geq d_{\min}(w)$$

That is, the minimum distances of windows popped from the priority queue are *monotonously* increasing.

Inactive Region Formation. To compute geodesics, windows are organized as the wavefront and propagated from near to far. Let w_n be the nearest window on the wavefront. It can be inferred with the *monotonicity* that the geodesic distance of a point p is determined if it is shorter than $d_{\min}(w_n)$. To apply this to forming the inactive region, the upper bound of points' distances within a triangle is estimated as $d_{\min}(f) + \|e_{\max}\|$, where $d_{\min}(f)$ is the minimum distance of face f , e_{\max} is f 's longest edge. Then, all the triangles f satisfying $d_{\min}(f) + \|e_{\max}\| \leq d_{\min}(w_n)$ form the inactive region (see Fig. 7). This process is summarized as Proposition 3.1 and its proof is shown in the Appendix.

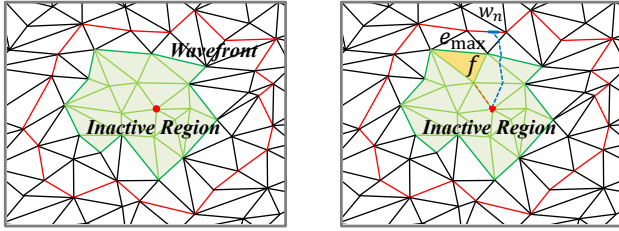


Figure 7: Illustration of an inactive region. Left: the segments in red denote the propagation wavefront w_f and the green shadowed area is the Inactive Region. Right: $d_{\min}(f)$ is the length of the orange path, e_{\max} is the longest edge of face f , $d_{\min}(w_n)$ is the length of the blue path.

Proposition 3.1 The inactive region is formed by all triangles satisfying $d_{\min}(f) + \|e_{\max}\| \leq d_{\min}(w_n)$ and none of the windows in it can be updated by later window propagations.

Proof See Appendix B. \square

Redundant Windows Removal (RWR) Redundant windows always appear within inactive regions. Thus, RWR works on inactive regions. Let f be a redundant triangle for removal, $d = d_{\min}(w_n)$ be the distance of the nearest window on the propagation wavefront. Then, RWR is performed in two steps:

Step 1. Judge if f is in the inactive region with Proposition 3.1. If so, continue to Step 2; else, finish.

Step 2. Check f 's redundancy with Definition 3.1. If f is redundant, also check if its edges are redundant and remove all windows on the redundant edges.

This process is summarized in Procedure 1.

3.3. Performance Verification

To verify that the proposed RWR procedure effectively reduces memory cost, this section compares memory costs against nearest distance $d_{\min}(w_n)$ of the wavefront between two scenarios of

Procedure 1 Redundant Windows Removal (RWR)

Input: f - Face;

d - Distance of the nearest window on the wavefront;

Output: f' - The face after redundancy removal;

```

1: procedure RWR( $f, d$ )
2:   Let  $e_{\max}$  be the longest edge of  $f$ ;
3:   if  $d_{\min}(f) + \|e_{\max}\| \leq d$  then
4:     Check  $f$ 's redundancy;
5:     if  $f$  is redundant then
6:       for each edge  $e_i \in f$  do
7:         Let  $f_i$  be the face sharing edge  $e_i$  with  $f$ ;
8:         if  $f_i$  is redundant then
9:           Empty the windows on  $e_i$ ;
10:        end if
11:      end for
12:    end if
13:  end if
14: end procedure

```

Voronoi diagram construction: with and without RWR. The tests are performed on ten models selected from the model set.

Fig. 8 shows the results on two models (Armadillo and Asian Dragon) and the rest of the results have been included in the supplementary materials. It can be seen that applying RWR dramatically reduces the memory cost of Voronoi diagram construction. Specifically, methods without RWR (e.g. [LCT11]) store all propagated windows on edges of the mesh and their memory costs are *cumulative*. On the contrary, RWR removes redundant windows in time with geodesic wavefront propagations. Thus, the memory cost is effectively reduced.

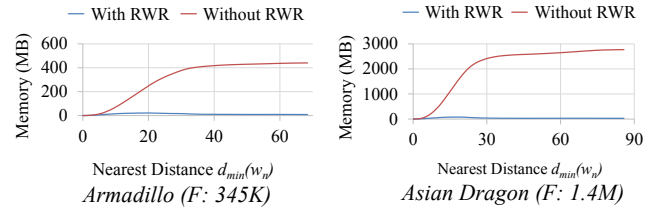


Figure 8: Performance verification on RWR. The x-axis represents the distance of the nearest window on the wavefront during propagation, i.e. $d_{\min}(w_n)$. The y-axis represents real-time memory cost during propagation.

4. Applying RWR in Geodesic Computation

To construct geodesic-metric-based Voronoi diagrams, we propose the *window-VTP* algorithm by revising the original VTP algorithm [QHY*16]. The overall workflow is shown in Fig. 9. Our algorithm is essentially a multi-source geodesic algorithm and takes triangles as the primitive for distance propagation. For each source, all visited triangles form its own traversed area. We define the boundary of the traversed area as the propagation wavefront.

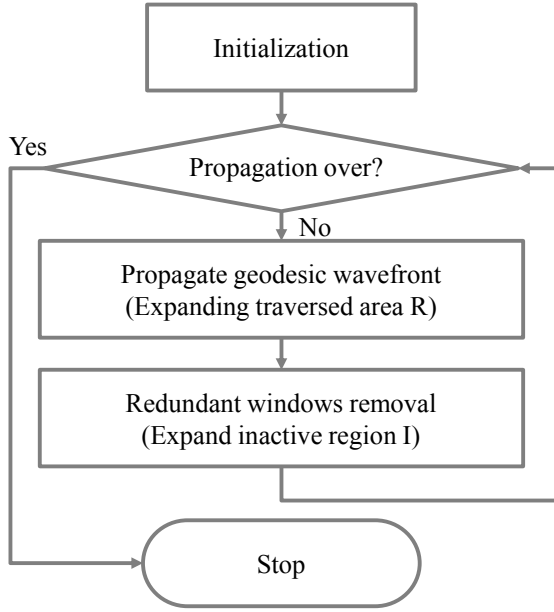
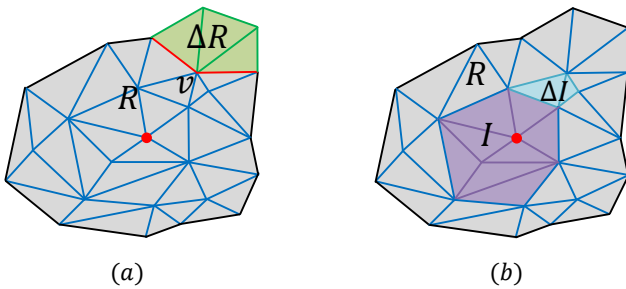


Figure 9: window-VTP algorithm workflow.

For simplicity, consider the one source scenario here. Our algorithm expands its traversed area R and inactive region I at the same time (Fig. 10). Note that the **inactive region** I is a *proper subset* of the **traversed area** R , i.e. $I \subset R$, and the windows in I will not be updated. Both R and I are expanded in continuous Dijkstra style, and gradually involving unvisited triangles abutting the wavefront. First, the proposed algorithm creates the initial windows of each source within its 1-ring neighbourhood and pushes all the adjacent vertices of each source into a priority queue Q . Note that we only define *one* priority queue Q for all traversed areas since every vertex is involved in Q in terms of the propagation distance of the wavefront. When a vertex is popped from the priority queue Q , the

Figure 10: Illustration of the triangle-oriented region expansion scheme. (a) Expansion of the traversed area R . (b) Expansion of the inactive region I .

proposed window-VTP algorithm performs the following:

- **Expanding traversed area R .** As Fig 10 (a) shows, let ΔR be

the unvisited triangles in v 's 1-ring neighbourhood. Then, R is expanded by involving ΔR into R , and the wavefront is also updated accordingly. Then, the windows on the previous wavefront (e.g. vE and vB in Fig. 11) are propagated through ΔR and R either till they reach the wavefront, or are eliminated during propagation. To manage windows on the wavefront for the Voronoi diagram construction, the propagated windows are trimmed on edges using the windows trimming and binary insertion methods proposed by the MMP algorithm [SSK*05].

- **Expanding Inactive region I .** As Fig. 10 (b) shows, the expansion of I is limited inside R . In the region between I and R , let ΔI be the triangles satisfying Proposition 3.1. Then, I is expanded by involving ΔI in I . When a triangle is added into I , the windows on it are removed by performing procedure $RWR()$.

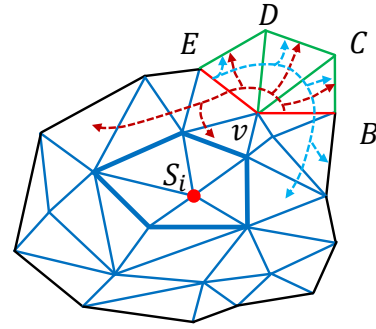


Figure 11: Vertex-sorted Triangle Propagation [QHY*16].

The outline of our algorithm is shown in Algorithm 2.

Two challenges are rising as below.

1. How to deal with the collision of the wavefronts? Note that it may be a self-intersection of one wavefront or meeting of two wavefronts.
2. How to define the priorities for triangles and vertices in Q_i and Q properly (in Step 4, 5)?

4.1. Wavefront Collision

Proposition 4.1 The proposed window-VTP algorithm automatically handles the wavefront collisions and requires no extra operations.

As Fig. 12 shows, the propagation wavefront consists of different parts corresponding to different sources. When different parts of the wavefront collide with each other, we simply let the windows propagate through the wavefront and enter the interior of the traversed areas. The propagations of these windows will stop when they reach the updated wavefront or be eliminated by the retained windows on edges in the traversed areas using the windows trimming rule [SSK*05]. Thus, no extra operation is required. For example in Fig. 12, the wavefront collides when ΔABC is added to the traversed areas. Then, the windows on edges AB , AC , BC are propagated into the interior of R_1 , R_2 and R_3 (the dashed arrows in Fig. 12). These propagations will stop upon reaching the updated wavefront (the bold red, green, blue line segments in Fig. 12) or be eliminated on the interior edges (the grey line segments in Fig. 12).

Algorithm 2 *window-VTP algorithm*

Input: M - Mesh;
 S - Source set;

Output: M' - Mesh with sufficient geodesic information for Voronoi diagram constructions;

```

1: procedure window-VTP( $M, S$ )
2:   Step 0. Perform Initialization.
      • For each source  $S_i$ , create a single window for every opposite edge of  $S_i$  in its 1-ring neighborhood (bold blue lines around  $S_i$  in Fig. 11).
      • Push all adjacent vertices of  $S_i$  into a priority queue  $Q$ .
      • Define a priority queue  $Q_i$ , which is used to organize the expansion of the inactive regions;
3:   while ! $Q.empty()$  do
4:     Step 1. Pop a vertex  $v$  from  $Q$ ;
5:     Step 2. Update the wavefront and traversed areas;
6:     Step 3. Expanding the traversed areas.
      • Push the windows on edges of the wavefront incident to  $v$  into FIFO queue  $W$ ;
7:     while ! $W.empty()$  do
8:       • Pop a window  $w$  from  $W$ ;
      • Propagate  $w$  across a triangle;
      • Retain and trim the propagated windows;
      • Push the propagate windows into  $W$  if they survives the trimming and haven't reached the wavefront;
9:     end while
10:    Step 4. Expanding the inactive regions.
11:    while ! $Q_i.empty()$  do
12:      • Let  $f$  be  $Q_i.front()$ ;
      • Perform  $RWR()$  on  $f$  to check if  $f$  is in the inactive regions; If so, remove the redundant windows on it; else, break the loop;
13:    end while
14:    Step 5. Update vertices' and triangles' priorities;
15:    Step 6. Push the faces newly added to the traversed areas into  $Q_i$ ;
16:  end while
17: end procedure

```

4.2. Priorities Definition

The key point of performing the procedure $RWR()$ during wavefront propagation is to form the **inactive region**, which resort to two priorities: the face's priority and the vertex's. Recall that the inequality of $d_{\min}(f) + \|e_{\max}\| \leq d_{\min}(w_n)$ is used to identify whether a face f is in the inactive region (Proposition 3.1). In our algorithm, the priorities are defined as follows:

Face's Priority. A face f 's priority in the priority queue Q_i is defined as $-(d_{\min}(f) + \|e_{\max}\|)$.

Vertex's Priority. A vertex v 's priority in the priority queue Q is defined as the negative minimum of the current shortest distances to v 's incident edges on the wavefront. For example in Fig. 13, $-d_{\min}(A) = -\min\{d_{\min}(AB), d_{\min}(AC)\}$. In addition, if w_n is on AB or AC , $-d_{\min}(A) = -d_{\min}(w_n)$.

Note that the two defined priorities are just the left and right sides

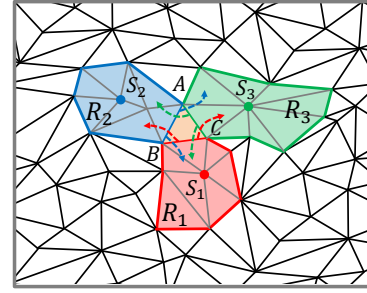


Figure 12: The collision of the propagation wavefront. The wavefront consists of three parts from three different sources, S_1 , S_2 and S_3 (red, blue and green line segments).

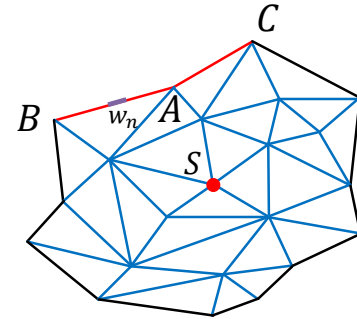


Figure 13: Illustration of the vertex's priority definition. The propagation wavefront are the black and red line segments. w_n is the nearest window on the wavefront.

of inequality $d_{\min}(f) + \|e_{\max}\| \leq d_{\min}(w_n)$ (Proposition 3.1), and thus they can be directly used when performing procedure $RWR()$.

5. Complexity Analysis

This section focuses on the complexity of geodesic computation since it is the dominant part of the Voronoi diagram construction [LCT11].

Let n be the number of vertices on a mesh. It is easy to verify that the proposed *window-VTP* algorithm is an improved version of the original MMP algorithm [MMP87]. In the worst case, the number of windows generated in the geodesic computation part is $O(n^2)$ and the time complexity of geodesic computation is $O(n^2 \log n)$. For the redundant windows removal (RWR) part, the checking and deletion processes are performed on each window and thus accounts for $O(n^2)$ time. In addition, the expansion of the inactive region is triangle-oriented and thus costs $O(n \log n)$ time for $O(n)$ triangles.

In summary, the time complexity of *window-VTP* is bounded by $O(n^2 \log n + n^2 + n \log n) = O(n^2 \log n)$. Since the redundant windows removal process does not consume extra memory, the space complexity of the proposed algorithms is bounded by $O(n^2)$.

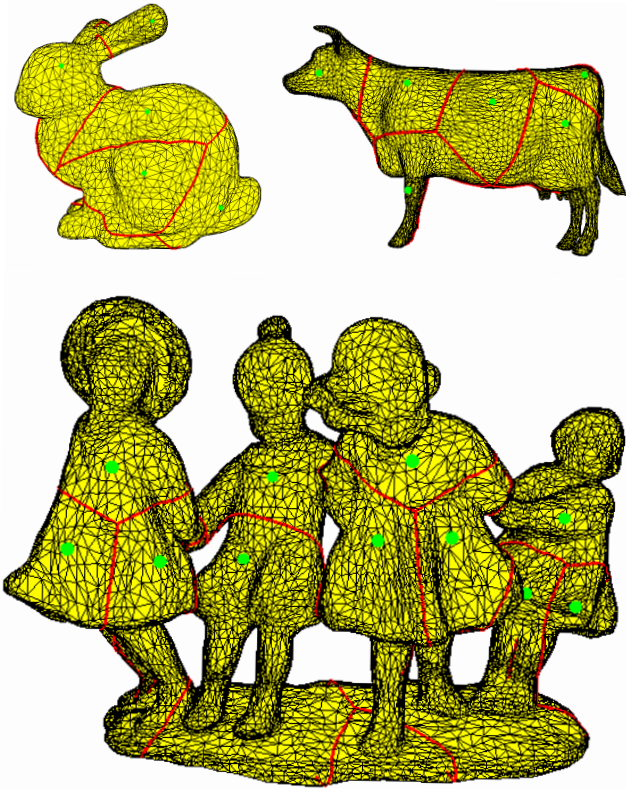


Figure 14: Examples of Voronoi diagrams on meshes. The faces of the models are: Bunny (5K faces), Cow (10K faces), Dancingchildren (20K faces).

6. Experimental Results

To evaluate the performance of the proposed algorithm, experiments have been conducted on a variety of models. Specifically, the test models are selected from the model set proposed in [QHY*16], including sculptures, animals and manmade objects. The resolution of these models (number of faces) ranges from 10K to 14M. All the algorithms are tested using a HP Z420 Workstation with an Intel Xeon E5-1650 3.20GHz CPU and 32GB memory. Unless specified, the experiments randomly select 30 vertices as the sources on meshes, as shown in [LCT11]. Fig. 14 shows the constructed Voronoi diagrams on some example meshes.

6.1. Comparison with [LCT11]

Overall Performance According to [LCT11], constructing the geodesic-metric-based Voronoi diagram consists of two stages,

- **Stage 1.** Compute geodesic distance fields on edges of mesh M .
- **Stage 2.** Extract the valid triangles which contain Voronoi cells' boundaries. March them to track and reconstruct the boundaries of Voronoi cells' by linking the intersections between them and edges of M .

The overall performance of the proposed algorithm is evaluated by two measures on the two stages: running time and peak memory usage respectively. As Table 1 shows, the geodesic computation part consumes the majority of time and memory in both Liu et al.'s ([LCT11]) method and ours. However, when replacing the MMP algorithm used in [LCT11] by the proposed *window-VTP* algorithm for geodesic computation, the Voronoi diagram construction runs 3-8 times faster and uses 10-70 times less memory.

Model	Performance	Liu et al. (2011)	Ours	Ratio
Horse	Time(s)	1.966 + 0.015	0.66 + 0.015	2.93
(F: 96K)	Peak memory(MB)	109.40 + 0.035	9.98 + 0.035	10.93
Bunny	Time(s)	3.637 + 0.028	1.07 + 0.028	3.34
(F: 144K)	Peak memory(MB)	187.00 + 0.046	14.86 + 0.046	12.55
Igea	Time(s)	10.916 + 0.048	3.019 + 0.048	3.57
(F: 268K)	Peak memory(MB)	478.06 + 0.065	26.50 + 0.065	18.00
Armadillo	Time(s)	9.863 + 0.046	2.982 + 0.046	3.27
(F: 345K)	Peak memory(MB)	440.33 + 0.066	21.09 + 0.066	20.81
Pulley	Time(s)	23.917 + 0.115	5.345 + 0.115	4.40
(F: 392K)	Peak memory(MB)	792.08 + 0.086	39.69 + 0.086	19.91
Rocker arm	Time(s)	32.012 + 0.091	6.985 + 0.091	4.54
(F: 482K)	Peak memory(MB)	1013.34 + 0.099	41.50 + 0.099	24.36
Asian dragon	Time(s)	110.083 + 0.255	20.281 + 0.255	5.37
(F: 1,400K)	Peak memory(MB)	2770.81 + 0.143	76.75 + 0.144	36.04
IsidoreHorse	Time(s)	89.538 + 0.211	21.229 + 0.211	4.17
(F: 2,209K)	Peak memory(MB)	2574.06 + 0.189	46.79 + 0.189	54.79
Happy buddha	Time(s)	482.715 + 1.291	58.946 + 1.291	8.04
(F: 2,583K)	Peak memory(MB)	8218.60 + 0.406	161.98 + 0.406	50.61
Neptune	Time(s)	832.83 + 0.784	96.843 + 0.784	8.54
(F: 4,008K)	Peak memory(MB)	13070.70 + 0.262	176.30 + 0.262	74.03

Table 1: Performance comparison with [LCT11]. The results are shown in an addition manner as: “geodesic computation” + “Voronoi diagram construction”.

Since the geodesic computation part is the bottleneck of Voronoi diagram construction, a more comprehensive comparison on it is performed as follows.

Performance Comparison on Geodesic Computation To evaluate the performance of the geodesic part, three measures are used: running time, total number of windows stored after propagation and peak memory usage. Algorithms in this comparison have been tested on all 55 models in the model set. For better reading experience, some of the testing results are shown here and the others are given in the supplementary materials.

	MMP vs. window-VTP	FWP-MMP vs. window-VTP
Time	3.98/1.55	1.21/0.18
# windows stored	48.96/38.98	48.96/38.99
Peak Memory	21.24/15.16	21.24/15.16

Table 2: The mean and standard deviation of the performance ratios between other algorithms and the proposed *window-VTP* algorithm on running time, the number of windows stored and peak memory usage. The table value is shown in “mean / standard deviation” format.

The mean and standard deviation of performance ratios are calculated between MMP, FWP-MMP (the latest implementation of

the MMP algorithm [XWL*15]) and the proposed *window-VTP* algorithm. The details are shown in Table 2. It can be seen that *window-VTP* on average runs 4 times as fast as MMP and comparable to FWP-MMP (1.2 times faster). The *window-VTP* algorithm on average uses 95.29% less memory than MMP and FWP-MMP. Furthermore, the *window-VTP* algorithm stores 97.96% less windows than MMP and FWP-MMP algorithms after propagation, which shows that it removes redundant windows effectively. Note that the proposed *window-VTP* algorithm is impressive since it resolves the memory bottleneck of Voronoi diagram oriented computation of geodesics, whilst not sacrificing the speed. For example, it uses 95.29% less memory than FWP-MMP while still being 1.2 times as fast. Detailed results on 5 representative testing models are shown in Table 3.

Model	Performance	Algorithms		
		MMP	FWP-MMP	<i>window-VTP</i>
Bunny (F:144K)	Time(s)	3.637	1.27	1.07
	# windows stored	2,451,104	2,451,105	85,959
	Peak Memory(MB)	187.00	187.00	14.86
Rocker Arm (F:482K)	Time(s)	32.012	9.088	6.985
	# windows stored	13,282,080	13,282,139	271,040
	Peak Memory(MB)	1013.34	1013.35	41.50
Asian Dragon (F:1,400K)	Time(s)	110.083	28.247	20.281
	# windows stored	36,317,620	36,317,847	346,142
	Peak Memory(MB)	2770.81	2770.83	76.75
Neptune (F:4,008K)	Time(s)	832.83	173.055	96.843
	# windows stored	171,319,703	171,374,203	857,068
	Peak Memory(MB)	13070.70	13074.80	176.30
Lucy (F:14,464K)	Time(s)			806.118
	# windows stored	Out of memory	Out of memory	12,071,796
	Peak Memory(MB)			921.005

Table 3: Performance comparison between MMP, FWP-MMP and ours on five representative models.

Number of Sources This section studies how the proposed algorithm performs with varying number of sources. First, three test models (Maxplanck, Angel, RedCircularBox) are chosen. For each model, eleven sets of sources are chosen randomly whose sizes range from 1 to 1000. Then, the ratios between the running time, peak memory of FWP-MMP based Voronoi diagram construction algorithm and that of ours on all source sets are calculated. The experiments are designed to show how the ratios change with changing number of sources.

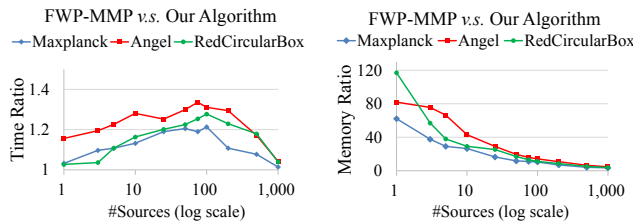


Figure 15: Performance comparison between FWP-MMP based Voronoi diagram construction algorithm and ours on the number of sources. The x-axis represents the number of sources in logarithmic scale, and the y-axis represents the performance (time, memory) ratio.

As illustrated in Figure 15, the time ratios increase within the range of source number at [1,100] and drop within the range at (100,1000]. This inconsistency is caused by RWR and the VTP wavefront propagation. When the number of sources increases,

- RWR is invoked less times. This is because the more triangles the Voronoi boundary occupies, the fewer the redundant windows.
- The performance of VTP wavefront propagation depends on the scale of the models, i.e. VTP performs better than the others on large scale meshes [QHY*16]. Herein, the size of Voronoi cells becomes smaller when the number of sources increases. VTP has to work within each cell, that is, the models' size becomes smaller for VTP.

The time ratio in Fig. 15 shows that in the range of [1,100], reducing RWR dominantly causes the time ratio increasing. In the range of (100,1000], the size of Voronoi cells becomes smaller, which leads to the performance of VTP decreasing. The low performance of VTP dominantly causes the time ratio decreasing at that time.

However, the memory ratio in Fig. 15 shows that the memory cost is close to that of FWP-MMP with an increasing number of sources. Nevertheless, the proposed algorithm still runs faster than the FWP-MMP based Voronoi diagram construction algorithm and uses more than 3 times less memory for 1000 sources.

Performance Profiling This section profiles the running time of different components in the Voronoi diagram construction, showing how it is accelerated. As proposed in [LCT11], the Voronoi di-

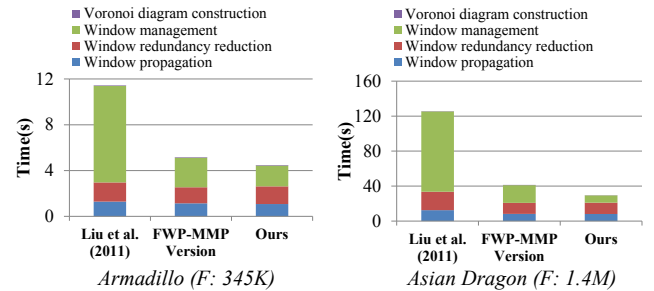


Figure 16: Comparison of running times of four common components in Voronoi diagram construction on two models. The comparison is performed on three versions of the solution: (1) the original method in [LCT11]; (2) the FWP-MMP version which replaces the MMP algorithm used in [LCT11] with the FWP-MMP algorithm [XWL*15]; (3) Our version which replaces the MMP algorithm used in [LCT11] with the proposed *window-VTP* algorithm.

agram construction contains two components: the computation of geodesics and the construction of a Voronoi diagram. In addition, the *geodesic computation* component can be further subdivided into three components [QHY*16]:

- **Window propagation** This component performs window propagations across the faces of a mesh.
- **Window redundancy reduction** This component identifies the redundant windows and removes them during propagation, including the window trimming and RWR processes.

- **Window management** This component manages the window propagations in order, which makes the *window redundancy reduction* component more effective. In the proposed algorithm, the VTP framework [QHY*16] is employed to propagate the window lists and remove the redundant ones (RWR) according to their distances, which is implemented by sorting vertices and faces in priority queues. Compared to the MMP and FWP-MMP [SSK*05, XWL*15] algorithms, the proposed algorithm achieves low window management overhead by sorting $O(n)$ vertices/faces instead of $O(n^2)$ windows in the priority queue, where n is the number of vertices on the mesh.

The running times of these four individual components in all participating algorithms are profiled on ten models selected from the model set.

Fig. 16 shows the results on two models, Armadillo and Asian Dragon (the rest of the results have been included in the supplementary materials). Compared to the *geodesic computation* components, the time cost of *Voronoi diagram construction* is extremely small and can be neglected. For *geodesic computation* components, it can be seen that the VTP framework effectively reduces the window management cost of the Voronoi diagram construction by sorting vertices or faces in the priority queue rather than windows. Furthermore, although an extra RWR process is added in our method, the running time of the window redundancy reduction component is not dramatically increased as its time cost is small compared to other computations (e.g. binary insertion and windows trimming).

Scalability First, three test models (Cow, Shark and Knot) are chosen. Let each of them have six different resolutions through subdivision. The number of faces ranges from 0.1M to 2M in these subdivided models. For each model, its ratios between the running time,

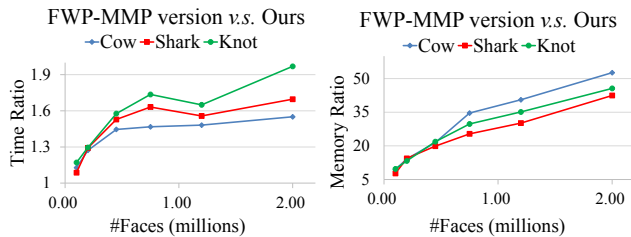


Figure 17: Comparison of scalability against FWP-MMP based Voronoi diagram construction algorithm. The x-axis represents the mesh resolution, and the y-axis represents running time ratio or memory cost ratio.

peak memory of FWP-MMP based Voronoi diagram construction algorithm and that of ours on all six resolutions is calculated. The experiments are designed to show how the ratios change with the changing resolution. As illustrated in Fig. 17, both the timing ratios and memory cost ratios increase with an increasing resolution. As shown, the rate of increase in performance for the proposed algorithm is proportional to the size of the models.

Robustness This section further validates that the proposed algorithm is robust to mesh triangulation quality. As in FWP [XWL*15], a sequence of meshes (eight) with different degrees

of anisotropy but a fixed resolution on two testing models (Fertility with 800K faces and Hand with 200K faces) are created respectively. Here, $g(M) = \frac{\sum_{f \in F} g'(f)}{|F|}$ is also used to measure the degree of anisotropy of a mesh M , where $g'(f) = \frac{PH}{2\sqrt{3}S}$ and P, H, S are the half-perimeter, longest edge length and area of f respectively. All these meshes with varied degrees of anisotropy are generated using the method in [ZGW*13].

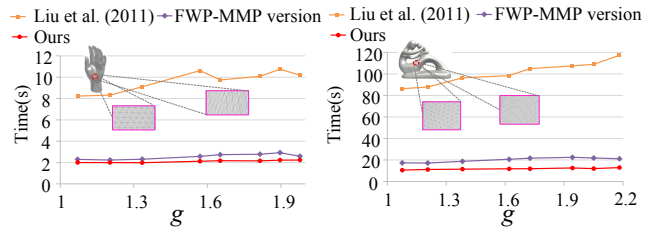


Figure 18: Comparison of robustness against anisotropic triangulation (Time). The x-axis represents the degree of anisotropy, and the y-axis represents running time.

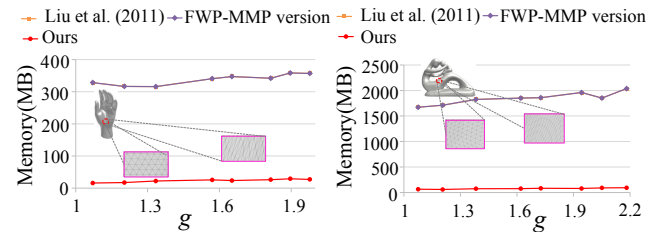


Figure 19: Comparison of robustness against anisotropic triangulation (Memory). The x-axis represents the degree of anisotropy, and the y-axis represents peak memory.

The curves in Fig. 18 and Fig. 19 show how the running times and peak memories change with increasing anisotropy (g) respectively. Note that the peak memories of Liu et al.'s method ([LCT11]) and its FWP-MMP based version are almost the same since both of them store all propagated windows on edges. The proposed window-VTP algorithm is the most robust among all algorithms since its running time and peak memory does not obviously increase when the input mesh has a much larger anisotropy.

6.2. Comparison with [XLS*14]

As Xu et al. have used the MMP algorithm to compute geodesics [XLS*14], its performance has already been compared in the preceding section and thus not discussed here.

Xu et al. proposed another method to reduce the memory cost of Voronoi diagram construction rather than the proposed RWR technique [XLS*14]. The main deficiency in their method is the *inefficiency* of the redundancy check. In their method, the redundancy check is performed on all unlabelled triangles rather than

Model	Performance	<i>window</i> -VTP + Xu et al. (2014) ($c = 1$)	Ours
Horse	Time(s)	1.16	0.68
(F: 96K)	Peak memory(MB)	13.38	10.01
Bunny	Time(s)	1.93	1.10
(F: 144K)	Peak memory(MB)	19.95	14.90
Igea	Time(s)	5.42	3.07
(F: 268K)	Peak memory(MB)	35.97	26.56
Armadillo	Time(s)	5.04	3.03
(F: 345K)	Peak memory(MB)	33.75	21.16
Pulley	Time(s)	12.60	5.46
(F: 392K)	Peak memory(MB)	58.17	39.78
Rocker arm	Time(s)	12.41	7.08
(F: 482K)	Peak memory(MB)	63.53	41.60
Asian dragon	Time(s)	42.17	20.54
(F: 1,400K)	Peak memory(MB)	132.99	76.90
IsidoreHorse	Time(s)	29.73	21.51
(F: 2,209K)	Peak memory(MB)	128.62	46.98
Happy buddha	Time(s)	160.47	60.24
(F: 2,583K)	Peak memory(MB)	493.70	162.39
Neptune	Time(s)	195.45	97.63
(F: 4,008K)	Peak memory(MB)	514.98	176.56

Table 4: Performance comparison with [XLS*14].

just the ones in the *inactive region* (Proposition 3.1). Thus, windows on many triangles are repeatedly checked since they are not inactive and will be updated by later propagated windows. In addition, since the cost of their redundancy check is large, performing it frequently is time-consuming. Thus, their method suffers from the *trade-off* between running time and memory-cost. In more details, they perform one redundancy check with every cn window propagations, where n is the face number of the mesh and c is a *user-defined* parameter to balance the performance. A smaller c means that the redundancy check is performed more frequently, reducing memory cost but sacrificing the running time.

On the contrary, the proposed RWR technique performs the redundancy check efficiently in the *inactive region* every time a vertex is popped from the priority queue. To make a fair comparison, we compare our algorithm with an improved version of [XLS*14] which uses the proposed *window*-VTP for geodesic computation but still employs their redundancy reduction method rather than our RWR (Table 4). In the experiments, we set the parameter c as 1 for a balanced performance. It can be seen that our algorithm outperforms [XLS*14] in both running time and peak memory.

6.3. Comparison with [QHY*16]

The original VTP algorithm does not retain windows, while the revised version keeps partial windows. Compared to the original VTP, this experiment shows how the change influences the performance.

As [QHY*16], in this experiment, we compare the performance using the proposed *window*-VTP with the original VTP to solve the *single-source discrete geodesic problem*, with the first vertex set as the source on the mesh. As Table 5 shows, our method runs approximately two times slower than VTP. The main reason is that the *window*-VTP has to strictly sort windows on edges by binary insertion. However, Voronoi diagrams are usually more sparse than meshes and there is no distinct decline in performance.

Model	Performance	VTP	Ours
Horse	Time(s)	0.64	1.13
(F: 96K)	Peak memory(MB)	1.25	5.67
Bunny	Time(s)	0.88	1.50
(F: 144K)	Peak memory(MB)	1.08	4.56
Igea	Time(s)	2.04	4.11
(F: 268K)	Peak memory(MB)	2.00	9.10
Armadillo	Time(s)	1.68	2.68
(F: 345K)	Peak memory(MB)	1.31	5.62
Pulley	Time(s)	3.97	8.71
(F: 392K)	Peak memory(MB)	4.53	18.58
Rocker arm	Time(s)	4.26	9.32
(F: 482K)	Peak memory(MB)	3.26	14.32
Asian dragon	Time(s)	9.74	20.95
(F: 1,400K)	Peak memory(MB)	3.72	16.77
IsidoreHorse	Time(s)	10.41	17.72
(F: 2,209K)	Peak memory(MB)	2.76	12.19
Happy buddha	Time(s)	31.44	68.75
(F: 2,583K)	Peak memory(MB)	8.44	40.46
Neptune	Time(s)	51.62	91.14
(F: 4,008K)	Peak memory(MB)	14.42	37.26

Table 5: Performance comparison with VTP [QHY*16].

6.4. Application to Remeshing

Due to that the Delaunay triangulation of a point set S is the dual of its Voronoi diagram, the proposed algorithm can be applied to remesh the dense models reconstructed from range data. In this context, the number of sources is usually fairly large and reaches the order of hundreds. Fig. 20 shows the remeshing result of the Neptune model with 4K randomly selected sources.



Figure 20: Illustration of remeshing with the proposed algorithm.

To show the performance of our method, we compare it with the

FWP-MMP version of [LCT11] on six dense models selected from the dataset of [QHY*16], whose numbers of faces range from 1.4M to 6.4M. For each model, we randomly select 2K sources if its number of faces is less than 2M; otherwise, 4K sources are selected. As Table 6 shows, our method runs faster and uses much less memory than the FWP-MMP version of [LCT11] in the remeshing problem.

# Samples: 2000			
Model	Performance	FWP-MMP version	Ours
Asian dragon (F: 1,400K)	Time(s)	14.07	11.18
	Peak memory(MB)	863.93	170.65
Pensatore (F: 1,996K)	Time(s)	25.02	17.24
	Peak memory(MB)	1503.96	251.48
Seahorse (F: 2,014K)	Time(s)	23.24	17.26
	Peak memory(MB)	1455.77	230.63

# Samples: 4000			
Model	Performance	FWP-MMP version	Ours
Happy buddha (F: 2,583K)	Time(s)	28.21	23.48
	Peak memory(MB)	1690.61	310.59
Neptune (F: 4,008K)	Time(s)	52.26	39.07
	Peak memory(MB)	2925.16	422.98
Vase lion (F: 6,370K)	Time(s)	111.381	72.22
	Peak memory(MB)	5567.37	673.80

Table 6: Performance comparison with the FWP-MMP version of [LCT11] on remeshing.

7. Conclusion

In this paper, the RWR procedure is presented to reduce the memory cost of constructing the geodesic-metric-based Voronoi diagrams, in which windows on edges are grouped within the inactive regions so that they can be removed together in time. The proposed window-VTP algorithm incorporates the RWR procedure in the vertex-oriented wavefront propagation framework. As a result, the window-VTP algorithm effectively resolves the memory bottleneck of the Voronoi diagram construction while not sacrificing the speed. In terms of experiments, our algorithm runs 3-8 times faster than Liu et al.'s method [LCT11], 1.2 times faster than its FWP-MMP variant and more importantly uses 10-70 times less memory than both of them.

In addition, the proposed method may be extended to compute other distances (e.g. anisotropic geodesic distances) on surfaces. All the Dijkstra-like approaches depend on the monotonicity of distance propagation. Thus, if the monotonicity is required, our method can work well.

Acknowledgements

We would like to thank the anonymous reviewers for their valuable comments. This work was partially supported by the Royal Society Newton Mobility (Ref. IE151018) and EU H2020 RISE project-AniAge (Ref. 691215).

References

- [Aur91] AURENHAMMER F.: Voronoi diagrams—a survey of a fundamental geometric data structure. *ACM Comput. Surv.* 23, 3 (Sept. 1991), 345–405. 2
- [CM07] COEURJOLLY D., MONTANVERT A.: Optimal separable algorithms to compute the reverse euclidean distance transformation and discrete medial axis in arbitrary dimension. *IEEE Transactions on Pattern Analysis and Machine Intelligence* 29, 3 (March 2007), 437–448. 2
- [CWW13] CRANE K., WEISCHEDEL C., WARDETZKY M.: Geodesics in heat: A new approach to computing distance based on heat flow. *ACM Trans. Graph.* 32, 5 (Oct. 2013), 152:1–152:11. 2
- [HR08] HESSELINK W. H., ROERDINK J. B. T. M.: Euclidean skeletons of digital image and volume data in linear time by the integer medial axis transform. *IEEE Transactions on Pattern Analysis and Machine Intelligence* 30, 12 (Dec 2008), 2204–2217. 2
- [KS98] KIMMEL R., SETHIAN J. A.: Computing geodesic paths on manifolds. *Proceedings of the National Academy of Sciences* 95, 15 (1998), 8431–8435. 2
- [KS99] KIMMEL R., SETHIAN J. A.: Fast voronoi diagrams and offsets on triangulated surfaces. In *Proc. of AFA Conf. on Curves and Surfaces* (1999), University Press, pp. 193–202. 2
- [LCT11] LIU Y., CHEN Z., TANG K.: Construction of iso-contours, bisectors, and voronoi diagrams on triangulated surfaces. *Pattern Analysis and Machine Intelligence, IEEE Transactions on* 33, 8 (Aug 2011), 1502–1517. 1, 2, 4, 6, 7, 8, 9, 11
- [MMP87] MITCHELL J. S. B., MOUNT D. M., PAPADIMITRIOU C. H.: The discrete geodesic problem. *SIAM Journal on Computing* 16, 4 (1987), 647–668. 2, 3, 6
- [NLC02] NA H.-S., LEE C.-N., CHEONG O.: Voronoi diagrams on the sphere. *Computational Geometry* 23, 2 (2002), 183 – 194. 2
- [OI03] ONISHI K., ITOH J.-I.: Estimation of the necessary number of points in riemannian voronoi diagram. In *Proc. 15th Canadian Conf. Comput. Geom* (2003), pp. 19–24. 2
- [OT95] ONISHI K., TAKAYAMA N.: Construction of voronoi diagram on the upper half-plane. *IEICE Transactions* 79 (1995), 533–539. 2
- [PC06] PEYRÉ G., COHEN L. D.: Geodesic remeshing using front propagation. *International Journal of Computer Vision* 69, 1 (2006), 145. 1
- [PM15] PEETHAMBARAN J., MUTHUGANAPATHY R.: Reconstruction of water-tight surfaces through delaunay sculpting. *Computer-Aided Design* 58 (2015), 62 – 72. Solid and Physical Modeling 2014. 1
- [QHY*16] QIN Y., HAN X., YU H., YU Y., ZHANG J.: Fast and exact discrete geodesic computation based on triangle-oriented wavefront propagation. *ACM Trans. Graph.* 35, 4 (July 2016), 125:1–125:13. 1, 2, 4, 5, 7, 8, 9, 10, 11
- [SSK*05] SURAZHISKY V., SURAZHISKY T., KIRSANOV D., GORTLER S. J., HOPPE H.: Fast exact and approximate geodesics on meshes. *ACM Trans. Graph.* 24, 3 (July 2005), 553–560. 1, 2, 5, 9
- [XLS*14] XU C., LIU Y.-J., SUN Q., LI J., HE Y.: Polyline-sourced geodesic voronoi diagrams on triangle meshes. *Comput. Graph. Forum* 33, 7 (Oct. 2014), 161–170. 2, 9, 10
- [XW09] XIN S.-Q., WANG G.-J.: Improving chen and han's algorithm on the discrete geodesic problem. *ACM Trans. Graph.* 28, 4 (Sept. 2009), 104:1–104:8. 1, 2
- [XWL*15] XU C., WANG T., LIU Y.-J., LIU L., HE Y.: Fast wavefront propagation (fwp) for computing exact geodesic distances on meshes. *Visualization and Computer Graphics, IEEE Transactions on* 21, 7 (July 2015), 822–834. 1, 2, 8, 9
- [ZGW*13] ZHONG Z., GUO X., WANG W., LÉVY B., SUN F., LIU Y., MAO W.: Particle-based anisotropic surface meshing. *ACM Trans. Graph.* 32, 4 (July 2013), 99:1–99:14. 9

Appendix A: Lemma A.1

Lemma A.1 Given a triangle whose three edges' lengths are a , b and c respectively. Let l be the length of a line segment in the triangle. Then, $l \leq \max(a, b, c)$.

Proof As Fig. 21 shows, let pq be a line segment in $\triangle DEF$ that $\|pq\| = l$. If either of p and q is not on the edges of $\triangle DEF$, extend pq as GH so that both its endpoints are on the edges and $\|pq\| \leq \|GH\|$. Fix one endpoint of GH , e.g. G . It is known that the

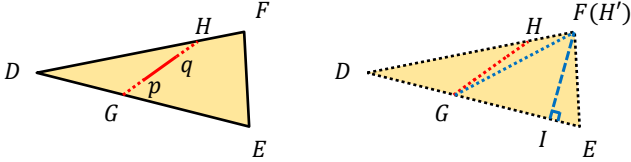


Figure 21: Illustration of Lemma A.1.

distance function over a line segment from G reaches extrema at the endpoints of the triangle edges, i.e. triangle vertices. Put H at any of such endpoints (e.g. F in Fig. 21) as H' and thus $\|GH\| \leq \|GH'\|$. Let I be a point on DE and $FI \perp DE$. Consider vertex $D \in \{D, E\}$ that D and G are on the same side of FI . It can be derived from the Pythagoras's theorem that $\|GH'\| \leq \|DF\|$:

$$\|GH'\|^2 = \|GI\|^2 + \|FI\|^2 \leq \|DI\|^2 + \|FI\|^2 = \|DF\|^2 \quad (\text{A.1})$$

Summarizing the above inequalities, we have $l = \|pq\| \leq \|GH\| \leq \|GH'\| \leq \|DF\|$ that $\|DF\|$ is an edge of the triangle. Thus, pq cannot be longer than the largest edge of $\triangle DEF$. \square

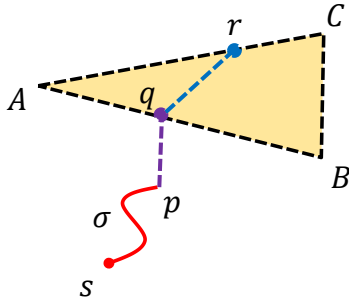
Appendix B: Proof of Proposition 3.1

Figure 22: Illustration of Proposition 3.1.

Proof Let f be a face satisfying $d_{\min}(f) + \|e_{\max}\| \leq d_{\min}(w_n)$ and q is the point determining $d_{\min}(f)$, i.e. $d_{\min}(f) = \delta + \|pq\| = d(q)$ (Fig. 22).

Let r be an arbitrary point in any window on the edges of f , construct a path to r by linking q and r with a line segment. Then, the geodesic distance $d(r)$ of r must not be larger than the length of the constructed path, i.e. $d(r) \leq d_{\min}(f) + \|qr\|$. Since $\|qr\| \leq \|e_{\max}\|$ (Lemma A.1),

$$\begin{aligned} d(r) &\leq d_{\min}(f) + \|qr\| \\ &\leq d_{\min}(f) + \|e_{\max}\| \end{aligned}$$

Knowing that f satisfies $d_{\min}(f) + \|e_{\max}\| \leq d_{\min}(w_n)$, then

$$d(r) \leq d_{\min}(w_n).$$

Thus, $d(r)$ cannot be updated by w_n since w_n cannot provide a shorter distance to r .

Let w_o be any other window on the propagation wavefront that $d_{\min}(w_n) \leq d_{\min}(w_o)$. Then, according to the *monotonicity* of window propagations,

$$d_{\min}(w_n) \leq d_{\min}(w'_n)$$

$$d_{\min}(w_o) \leq d_{\min}(w'_o)$$

where w'_n and w'_o are child windows propagated from w_n and w_o respectively. Then, it can be derived that,

$$d(r) \leq d_{\min}(w_n) \leq d_{\min}(w'_n)$$

$$d(r) \leq d_{\min}(w_n) \leq d_{\min}(w_o) \leq d_{\min}(w'_o)$$

Thus, $d(r)$ cannot be updated by all later window propagations. Since r is arbitrarily selected, all windows on f 's edges will not be updated. \square